



Development of kinetic models for photocatalytic ozonation of phenazopyridine on TiO₂ nanoparticles thin film in a mixed semi-batch photoreactor



Mehrangiz Fathinia^a, Alireza Khataee^{a,*}, Soheil Aber^b, Abdolhossein Naseri^c

^a Research Laboratory of Advanced Water and Wastewater Treatment Processes, Department of Applied Chemistry, Faculty of Chemistry, University of Tabriz, 51666-16471 Tabriz, Iran

^b Research Laboratory of Environment Protection Technology, Department of Applied Chemistry, Faculty of Chemistry, University of Tabriz, 51666-16471 Tabriz, Iran

^c Department of Analytical Chemistry, Faculty of Chemistry, University of Tabriz, 51666-16471 Tabriz, Iran

ARTICLE INFO

Article history:

Received 11 January 2015

Received in revised form 22 June 2015

Accepted 21 November 2015

Available online 26 November 2015

Keywords:

Modeling

Ozonation

Pharmaceuticals

Photocatalysis

TiO₂ nanoparticles

ABSTRACT

The degradation of phenazopyridine hydrochloride (PhP), an analgesic pharmaceutical, through photocatalytic ozonation process was modeled using three types of kinetic approaches. The experiments were performed using a semi-batch photoreactor where TiO₂ nanoparticles thin film was coated on ceramic plates irradiated by UV-A light in the proximity of ozone. The surface morphology, topography and roughness of the bare and TiO₂ coated ceramic plates were analyzed using scanning electron microscopy (SEM) and atomic force microscopy (AFM). The photocatalytic ozonation kinetic characteristics were experimentally investigated under the different operational parameters including pH, PhP initial concentration, ozone inlet flow rate, light intensity, ozone and oxygen dissolved concentrations. It was found that the pseudo-first-order rate constant (k_{app}) decreased with increase in the initial PhP concentration and increased with increasing ozone inlet flow rate solution pH and light intensity. Based on the generally accepted intrinsic elementary reactions for photocatalytic ozonation process, a novel kinetic model was proposed and validated for predicting PhP removal efficiency. The developed kinetic model explicitly explains the dependency of the apparent kinetic constant on PhP initial concentration, light intensity, ozone and oxygen dissolved concentrations. A good agreement among the predicted values of PhP removal efficiency using the developed model with experimental results was observed ($R^2 = 0.987$, MSE = 0.0011 and MAE = 0.0290). In order to profoundly evaluate and compare the accuracy of the proposed intrinsic kinetic model, an empirical kinetic model as function of main functional parameters and an artificial neural network model (ANN) by 3-layer feed-forward back propagation network with topology 5:14:1 were developed. The performance of the three models was compared based on the error functions and analysis of variance (ANOVA). Comparison based on the errors function demonstrated that the experimental data were fitted reasonably well by all the three proposed models with an adequate accuracy. Also, ANOVA results showed that there is no significant discrepancy among the predicted values of the three proposed models, implying that the kinetic model have been developed based on the proper specification of the intrinsic reactions occurred in the process.

© 2015 Elsevier B.V. All rights reserved.

1. Introduction

Recently, a great number of pharmaceuticals and personal care products, prevalently known as emerging contaminants (ECs), are being detected through the aqueous systems such as rivers, lakes,

streams, aquifers and wastewater treatment plant influents and effluents. The above mentioned compounds are considered to be potentially hazardous as some are ubiquitous, persistent to conventional wastewater treatments. Most of the ECs are determined to have the endocrine disruption functions [1,2]. In fact, removal of these ECs from water can provide a remarkable contribution to water conservation with vital savings of water resources which is one of the primary purposes of sustainability [3]. It has been well known that advanced oxidation processes (AOPs) are able to

* Corresponding author. Fax: +98 41 33340191.

E-mail addresses: a.khataee@tabrizu.ac.ir, ar.khataee@yahoo.com (A. Khataee).

degrade ECs which are resistance to biological degradation [4,5]. Moreover, it has been well demonstrated that the combination of the various AOPs can lead to an enhanced production of the various oxidizing species such as hydroxyl radicals ($\cdot\text{OH}$) and, as consequence, to faster degradation of pollutants [6,7]. Therefore, investigations on these technologies have been continuously increasing recently. In this sense, ozone in combination with heterogeneous photocatalysts irradiated by the ultraviolet (UV) light is also called “photocatalytic ozonation” which has been demonstrated to be a promising AOP for water treatment [3,8]. In this process usually an n type semiconductor oxides particles such as TiO_2 nanoparticles are used as a heterogeneous catalyst. The light with radiation energy of greater than or equal to the band gap energy of the semiconductor activates the photocatalyst and causes to electron–hole pairs formation on its surface, which induces the redox reactions of the adsorbed species [9,10].

Through the mentioned process, a considerable increase in the rate of the oxidation and mineralization of organic substances was continuously reported. According to the findings and reports, the various previous researchers have already related this phenomenon to the synergistic effect which occurs when photocatalysis and ozonation are carried out simultaneously [1,11]. Likely explanation of this effect is that in the presence of ozone additional amount of $\cdot\text{OH}$ radicals are generated on the surface TiO_2 through the formation of an ozonide radical ion ($\text{O}_3^{\bullet-}$). This issue would lead to the notable enhancement in the oxidation of the pollutants [3]. This technique was successfully utilized for water treatment and would be suitable for accomplishing the complete degradation of organic and inorganic pollutants. Also, a considerable amount of studies have reported the successful removal of the various types of ECs by photocatalytic ozonation process [1,12]. Nevertheless, it should be stated that most of the above mentioned research attempts have been dedicated to investigate the effects of operational parameters on the removal efficiency of the various types of organics, explain the presence of synergy and study the mechanism of the process [13,14]. However, to the best of our knowledge, very few studies that are mainly concentrated on the kinetic modeling of contaminant degradation by photocatalytic ozonation process have been published [10,15,16]. As an example Beltran et al. [10], in their work for photocatalytic ozonation of diclofenac developed a kinetic model based on mole balance equation of main species in the process. The proposed model was able to predict the changes in the total organic removal with time at different operating conditions. Also, Dong et al. [9] proposed a kinetic model for predicting the concentration changes of phenol through their work for photocatalytic ozonation of phenol. To simplify the model for predicting the concentration changes of the pollutant under different operating conditions, the authors assumed that all the oxidations were single-step processes with first order reactions.

Moreover, since heterogeneous photocatalytic ozonation process is a complicated gas–liquid–solid–photolytic process including free radical and surface reaction steps, mass transfer and photochemical processes, the kinetic modeling of the process seems to be a challenging matter. So, development of the efficient kinetic models for photocatalytic ozonation process can be a useful tool for (i) better studying the process variables and (ii) determining the effective parameters for the process design. Also, practical application of the process postulates the determination of the design and functional variables [17,18].

For the heterogeneous photocatalytic ozonation process, TiO_2 nanoparticles were reported to be the most suitable semiconductor because of its chemical inactivity and non-photocorrosivity [19,20]. Many attempts have been made to develop supported photocatalysts, either in the form of fixed beds, fluidized beds or slurries. Among them, TiO_2 nanoparticles thin film coating on ceramic, sand

blasted glass and non-woven plates appeared to be the promising way to increase the recovery properties of the catalyst [3,5,21].

Therefore, in the present work, TiO_2 nanoparticles thin film on ceramic plates was prepared by a sol-gel based method and selected as a fixed photocatalyst for heterogeneous photocatalytic ozonation system. The surface morphology, topography, roughness and the film thickness were completely characterized by SEM and AFM analysis. PhP, an analgesic pharmaceutical, was used as a model EC. A novel intrinsic kinetic model for degradation of PhP by the photocatalytic ozonation process was established according to the generally accepted intrinsic elementary reactions of the photocatalytic ozonation process.

2. Materials and methods

2.1. Chemicals

PhP was purchased from Shahredar pharmaceutical company (Tehran, Iran). The investigated photocatalyst in the present work was Millennium TiO_2 PC-500 (anatase > 99%, crystallites mean size 8 nm) immobilized on ceramic plates. A detailed physicochemical characterization of the used photocatalyst can be found in the authors' previous published works [19,22]. Brunauer–Emmett–Teller (BET) surface area and the total pore volume of the used photocatalyst were determined as $320.76 \text{ m}^2/\text{g}$ and $0.3104 \text{ cm}^3/\text{g}$, respectively. All the reagents supplied by Merck Co. (Germany) had analytical grades and were used without further purification.

2.2. Preparation of the TiO_2 nanoparticles thin film on ceramic plate

Sol-gel dip-coating method was applied to immobilize TiO_2 nanoparticles on the ceramic plates. Through the present procedure, organically modified silica (Ormosil) was utilized as the hydrophobic binder. The coating solution was composed of 40 mL of methanol, 0.5 g of TiO_2 nanoparticles, and appropriate amount of methyltrimethoxysilane (MTMOS) which was adjusted to access the required TiO_2 /Ormosil weight ratio of 0.240. The HCl solution (1 M) was added to the hydrolysis of MTMOS. The obtained slurry was sonicated in a batch type sonicator for 15 min (Sonica, 2200 EP S3, Italy) with 50–60 Hz frequency [3].

2.3. Photoreactor and reaction procedure

Photocatalytic ozonation experiments were performed in a 2 L capacity completely mixed rectangular semi-batch borosilicate glass photoreactor. The photoreactor was supplied with four ceramic plates which were located on the four walls of the reactor. The outer surface of the ceramic plates was coated with TiO_2 nanoparticles. Also, it was provided with a mixer, inlet for ozone, a porous titanium plate placed at the reactor bottom, sampling port and outlet for the non-absorbed ozone gas. Ozone was generated from oxygen on demand in a homemade laboratory generator. Oxygen gas (1–5 L/min) provided by oxygen generator (Airsep, USA) was fed into the laboratory ozone generator. An ozone–oxygen mixture was continuously bubbled into the solution through a diffuser situated at the bottom of the reactor. The gas flow rate was changed from 1 to 9 L/h with an ozone-dissolved concentration between 0.33 and 4.35 mg/L. Artificial irradiation was provided by a four 24-W, 36-W, 40-W and 100-W, UV-A lamps (Philips, the Netherlands) which was positioned inside a quartz tube within the reactor. The UV-A radiation intensity of 24-W, 36-W, 40-W and 100-W lamps at the outer surface of the TiO_2 thin film catalyst was 15.30, 22.95, 25.50 and 40.05 W/m², respectively which

was measured by a UV radiometer purchased from Cassy Lab Company (Germany). For investigating the influence of different light intensities on the reaction kinetic the desired lamp was used.

2.4. Experimental conditions for kinetic analysis of the process

2000 mL of PhP solution was utilized at the desired concentration in all cases. To probe the dependence of the kinetic characteristics of the photocatalytic ozonation on the pH of solution, initial PhP concentration initial ozone inlet flow rate and UV light intensity a series of experiments were performed at different photocatalytic ozonation conditions. The light intensity of UV-A lamp was altered from 15.30 to 40.05 W/m². The initial pH of solution was varied from 3 to 7 with H₂SO₄, NaOH or buffered with appropriate concentration of NaH₂PO₄ and NaHCO₃. The initial concentration of PhP was changed from 25 to 45 mg/L. The inlet flow rate of ozone gas was altered from 1 to 9 L/h. The dissolved concentration of ozone and oxygen has been shown through the each applied ozone inlet flow rate in Table S1. Within the different intervals, samples of 5 mL were taken and 1 mL ethanol was added to the samples to extinguish any development of ozone or hydroxyl radical oxidation before the analytical determination of PhP. The remaining PhP was determined using a spectrophotometer at $\lambda = 436$ nm and drawing the calibration curve. Using this method, the percent of PhP removal efficiency (%) can be obtained. The PhP removal efficiency (%) is the percentage ratio of removed drug concentration to that of the initial one.

Dissolved ozone concentration was determined by the decolorization of a 5,5,7 indigotrisulphonate solution according to the method reported by Bader and Hoigne [23]. Dissolved oxygen concentration was monitored by using a DO meter sensor (WinLab, Art. 6103 30,001, Germany). Also, for more information about the analytical methods please see Supporting data.

3. Results and discussion

3.1. Analyses of the TiO₂ nanoparticles thin film on ceramic plate by SEM and AFM

The SEM analysis was used to investigate the exterior and cross-sectional morphologies of bare and TiO₂ nanoparticles coated ceramic plates (Fig. 1a–c). The highly rough and coarse surface with disordered valleys corresponding to the bare ceramic plate could be seen in Fig. 1a. Fig. 1b with the inset SEM graphs in different magnification present the surface morphology of the ceramic plate covered with a thin layer of TiO₂ nanoparticles. SEM images demonstrate that the produced thin layer is in the form of a network of high-porosity, inter-connected nanoparticles with the approximate particle size of around 40 nm. Also, it can be seen that due to the homogenous distribution of the nanoparticles inside the thin layer there is no cracks and visible agglomerates on the entire surface. Fig. 1c and its inset graph exhibit the thickness and the morphology of the particles in produced thin layer on the lateral side of the ceramic plate, respectively. The thickness of the produced film is about 170 μ m and it has been composed of a high number of granular micro zones which can be attributed to the aggregation of TiO₂ colloidal nanoparticles to a certain level.

AFM analysis was used to investigate the surface topography and roughness of the bare and TiO₂ coated ceramic plates. Fig. 2a–d shows the three and two-dimensional AFM images of the bare and TiO₂ coated ceramic plate. Through the mentioned figures, the brightest area demonstrates the highest point of the ceramic surface and the dark area displays the valleys or ceramic domes. Fig. 2a shows the three-dimensional AFM image of bare ceramic plate. From Fig. 2a, the irregular valleys and domes on the sur-

face of bare ceramic can be clearly observed. Also, two-dimensional AFM image (Fig. 2b) and the distribution plot (inset plot of Fig. 2b) confirm the erratic distribution of the valleys. Fig. 2c shows the three-dimensional AFM image of TiO₂ coated ceramic plate. This figure demonstrates that in consistency with SEM results, TiO₂ nanoparticles in the coated ceramic plate are distributed uniformly.

Moreover, as shown in Fig. 2c, TiO₂ nanoparticles thin film on the ceramic surface consists of the individual nanometric particles of 10–20 nm. Also, as depicted in the two-dimensional AFM image of the coated ceramic in Fig. 2d, the produced film is completely uniform on the entire surface. Through the distribution plot (inset plot of Fig. 2d) the widths of each peak can be seen. It can be observed that the width of each peak is about 27.2 nm. Also, the distance between the peaks is about 27.2 nm, which shows the homogeneous distribution of aggregated nanoclusters of 27.2 nm in the thin layer. Also, it can be concluded that nanoclusters were arranged methodically with the distance of 27.2 nm.

The quantitative measurement of the surface roughness parameters of the bare and TiO₂ coated ceramic plates which have been computed in an AFM scanning area of 272 nm \times 272 nm have been presented in Table 1. The surface of the bare ceramic was rather smooth with an average roughness value of 1.0729 nm. An increase in the S_a value to 9.207 nm and the production of spherical dome-like aggregates revealed the successful immobilization of TiO₂ nanoparticles on the surface of ceramic plate.

3.2. Comparison of different oxidation processes

Before beginning the functional evaluation of the parameters (initial concentration of pollutant, solution pH and ozone inlet flow rate), a series of tests were carried out to elucidate the contribution and effectiveness of different oxidation processes. Fig. 3a shows the removal efficiency of PhP toward the reaction time for the six oxidation processes. PhP removal is negligible by the direct photolysis under UV-A irradiation in the presence of oxygen. The PhP molecules can absorb radiation with the absorbance maximum value of 425 nm. However, the light source used in the study emitted radiation at the highest value of 354 nm, and hence this was why PhP did not degrade by the photolysis process. Fig. 3a illustrates that the removal of PhP by the photocatalytic process within 35 min is about 25%. According to the related literature, UV/TiO₂ process is rather a slow process and it needs more reaction time for completing the removal and mineralization of the organic pollutants [8,24]. Also, this can be explained by the fact that the recombination rate of electrons and positive holes on the photocatalyst surface in the presence of oxygen is rather high resulting in a decrease in the amount of hydroxyl radicals generated. The removal of PhP by the ozonation and photolytic ozonation at 35 min was about 58% and 63%, respectively. It should be stated that PhP degradation by ozonation and photolytic ozonation took place exclusively in the liquid phase through both direct and indirect mechanism process, which was discussed in Section (3.4.1). Fig. 3a shows that the removal efficiency of PhP increases by about 5% by photolytic ozonation process. The removal efficiency of PhP by the catalytic ozonation process was notably higher than that of the ozonation (about 71% at 35 min). This can be a sign for implementing the heterogeneous catalytic ozonation on the thin layer of TiO₂ coated on ceramic surface. Finally, from Fig. 3a it can be understood that the highest PhP removal efficiency was accessed in the photocatalytic ozonation process (about 95% at 35 min). Our findings are in agreement with the results of comprehensive studies of Beltran et al. dealing with the photocatalytic ozonation of different pollutants [13,25,26]. Moreover, according to the data accessed from Fig. 3a, it can be deduced that PhP degradation by photocatalytic ozonation occurs via two main pathways including oxidation in the liquid phase via both direct and indirect mechanism, and oxidation on the

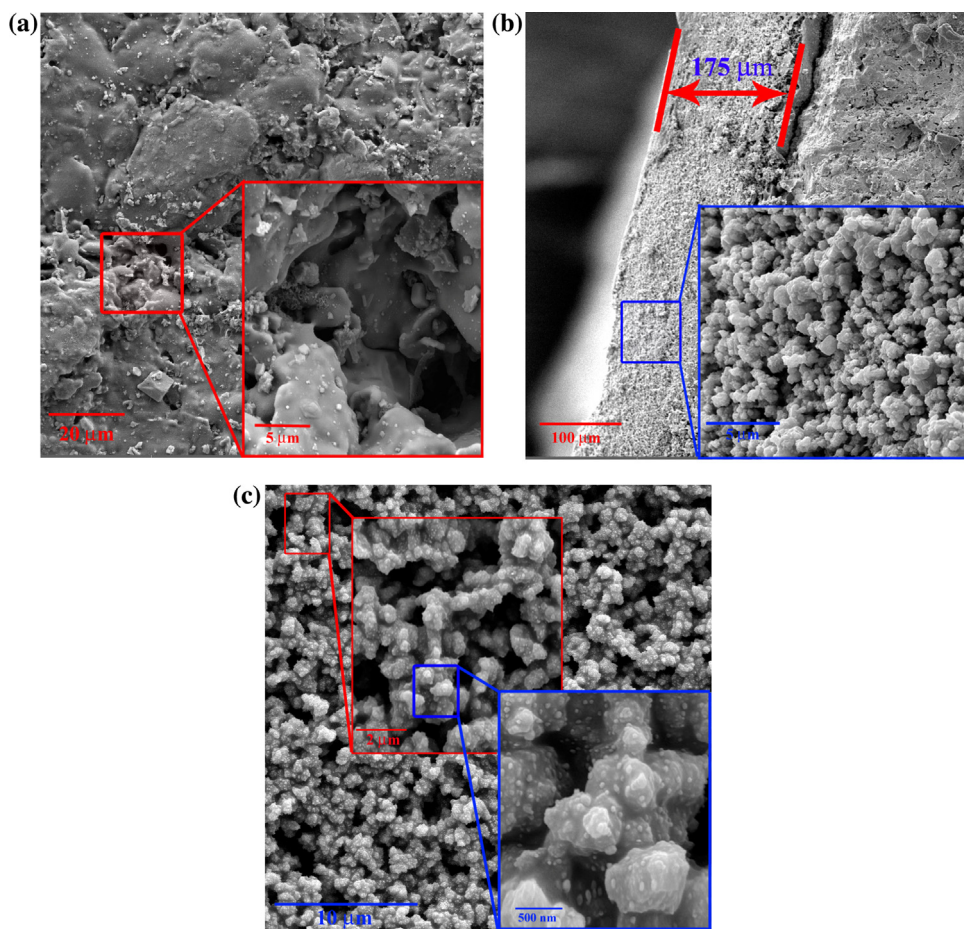


Fig. 1. (a) Surface SEM images of bare ceramic plate and (b and c) surface and cross sectional SEM images of TiO_2 nanoparticles thin film on ceramic plate.

Table 1

Area roughness parameters of the bare and TiO_2 coated ceramic plates resulted from analyzing three randomly selected AFM analysis.

Samples	Roughness parameters				
	S_a (nm)	S_q (nm)	S_y (nm)	S_p (nm)	S_m (pm)
Bare ceramic	1.072	1.380	15.405	8.562	27.833
TiO_2 nanoparticles coated ceramic	9.207	10.903	74.193	37.485	4.828

S_a : Average roughness.

S_q : Root mean square.

S_y : Peak-valley height.

S_p : Peak height.

S_m : Mean value.

surface of the catalyst by the adsorbed $\cdot\text{OH}$ radicals and its exact mechanism was discussed in Section (3.4.2).

Regarding the kinetic of the oxidation processes, it has been assumed that the concentration of the main oxidizing species such as ozone and OH was constant during the oxidation processes. So, the pseudo-first-order kinetics given in Eq. (1) can be applied to fit the obtained experimental data of the PhP removal efficiency in these processes.

$$r = -\frac{dC}{dt} = k_{\text{app}}C \Rightarrow \frac{C}{C_0} = \exp(-k_{\text{app}} \times t) \quad (1)$$

where k_{app} is the apparent first-order rate constant (with the same restriction of $C = C_0$ at $t = 0$, with C_0 being the initial concentration in the bulk solution after the dark adsorption), and t is the reaction time.

Fig. 3b was prepared according to Eq. (1). It should be stated that the correlation coefficients (R^2) in all plots were found to be higher

than 0.99, proving that the removal of PhP followed the proposed kinetic.

3.3. The effects of operational parameters on photocatalytic ozonation of PhP

Four different series of experiments were performed to investigate the influence of the pH of the solution, the initial concentration of PhP, the ozone inlet flow rate and the light intensity on removal of PhP. A plot of $\ln(C_0/C)$ versus time for all experiments has been shown in Fig. 4a-d. The experimental data of PhP degradation under the various operating conditions was well fitted with pseudo-first-order kinetic equation. It is obvious that the assessed parameters have impressive influence on PhP removal efficiency.

As it can be observed in Fig. 4a, k_{app} gradually increases with increasing of the pH value. This behavior can be explained considering the kind of interactions between PhP molecules and the

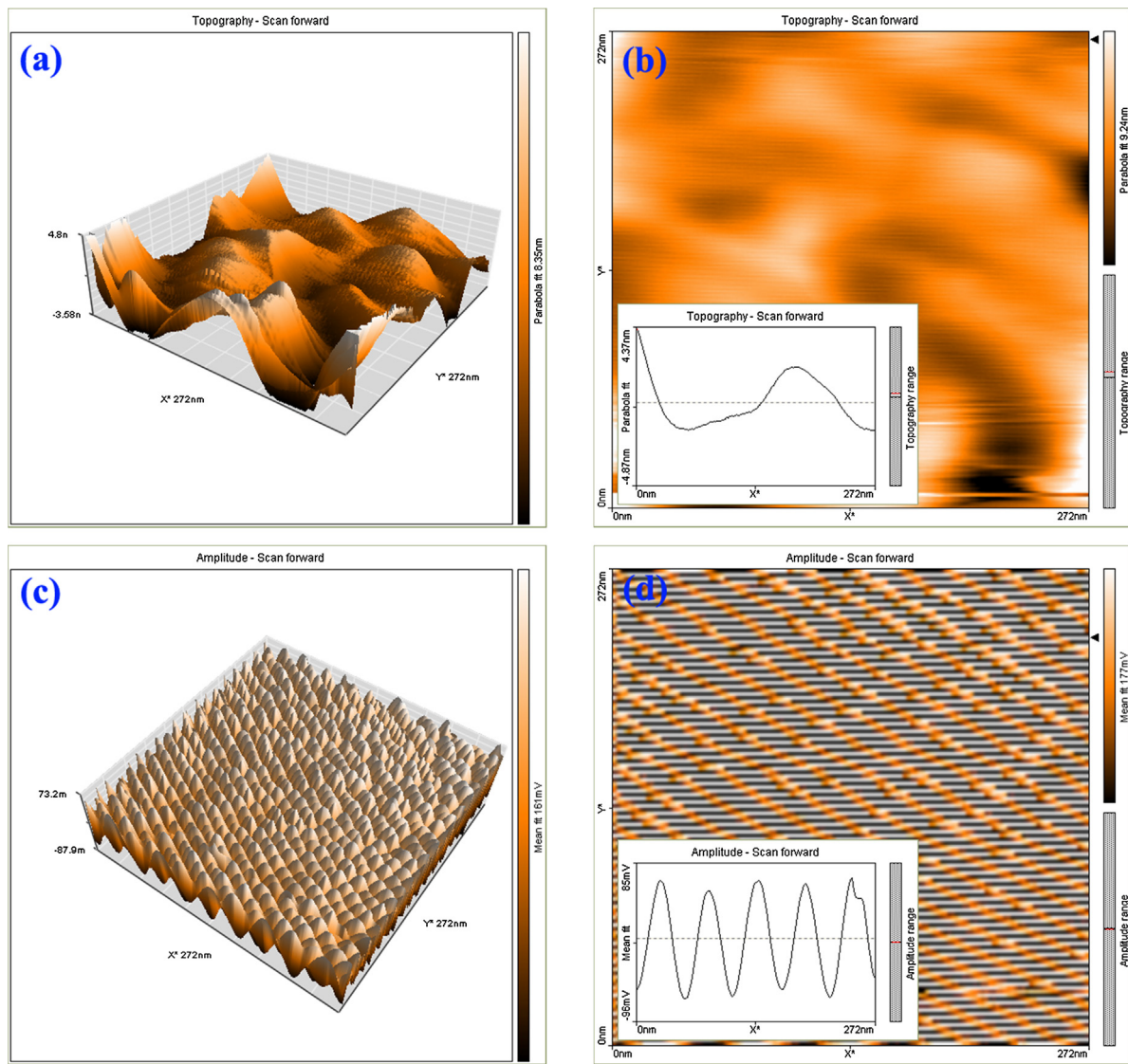


Fig. 2. (a and c) Three-dimensional (3D) AFM images of bare ceramic plate and TiO_2 nanoparticles thin film on ceramic plate, respectively and (b and d) two-dimensional (2D) top views and size distribution plots (inset plots) of bare ceramic plate and TiO_2 nanoparticles thin film on ceramic plate, respectively.

catalyst surface. Also, it has been well described that in photocatalytic ozonation process pH affects the surface charge properties of the organic pollutant, the adsorption behavior of TiO_2 and the stability of dissolved ozone molecules. Accordingly, the adsorption/desorption properties of the PhP and the stability of dissolved ozone molecules are a critical step in the photocatalytic ozonation process. At acidic pH conditions both PhP molecules and the surface of the catalyst are positively charged (the isoelectric point of TiO_2 nanoparticles surface is 6.3 [13] and the pK_a value of PhP is 5.12). Therefore, weak adsorption is related to the repulsing effect of two positive charges. At pH 5, the surface of TiO_2 is in positive form and the PhP can be in the neutral form. So, due to the increased adsorption, the degradation of PhP is enhanced. Also, according to the literature, increasing of k_{app} can be related to the synergistic effect by increase of pH from 3 up to 7; that is, under the mentioned pH conditions ozone molecules are anticipated to be stable in their molecular form rather than the decomposed form. Hence, ozone molecules are capable of forming $\text{O}_3^{\bullet-}$ (avoiding the recombination of electron (e^-) and oxidant positive hole (h^+) on the TiO_2 catalyst) by extracting the electrons from the conduction band of TiO_2 . Consequently it leads to the production of high amount of OH [5,25].

The investigation of ozone inlet flow rate (Fig. 4b) indicates that the pseudo-first-order rate constant increased with increasing of ozone inlet flow rate up to 9 L/h. Also, it is worth mentioning that, the dissolved ozone concentration in the solution changed between 0.3 and 5 mg/L as a function of altering the ozone inlet flow rate from 1 to 9 L/h (see Table S1). The possible reason for this phenomenon is related to the synergistic effect which leads to the increase in the production of OH in the process. By increasing of ozone inlet flow rate, the concentration of dissolved ozone is increased. The dissolved ozone molecules can easily adsorb on the surface of TiO_2 in its molecular or dissociative form via physical adsorption or formation of weak hydrogen bonds with surface hydroxyl groups. Ozone molecules capture electrons produced on TiO_2 surface which produce ozonide radical anion; consequently, the produced ozonide radical anion results in high amount of $\bullet\text{OH}$ formation which increases the removal rate constant of PhP [25,27]. Our research findings in the present study are consistent and compatible with the results of previous studies in the related literature [25,28,29], in which an increase in the ozone concentration in the inlet gas results in more effective removal of organic compounds in the photocatalytic ozonation process.

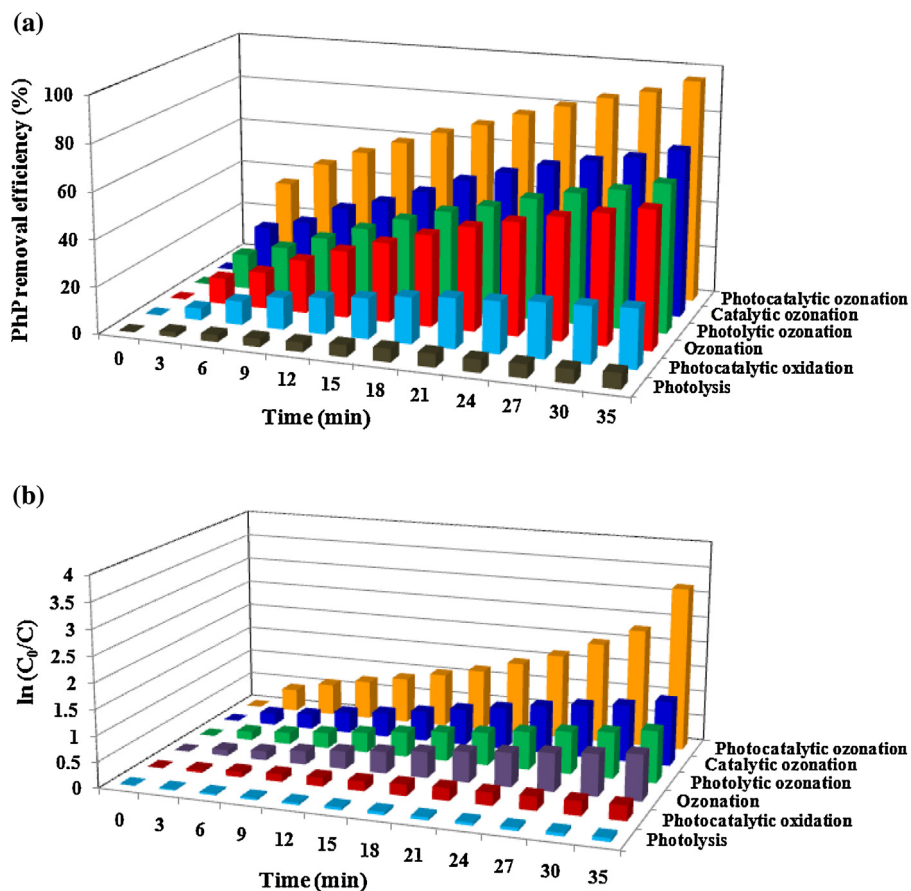


Fig. 3. (a) Time evolution of PhP removal efficiency (%) during various oxidation processes and (b) the corresponding kinetic analysis assuming a pseudo-first-order kinetic for degradation of PhP. Experimental conditions: [PhP]: 25 mg/L, ozone inlet flow rate: 5 L/h, pH buffered at pH 7 and light intensity: 40.05 W/m².

As depicted in Fig. 4c, the pseudo-first order removal rate constant decreases with increasing of PhP initial concentration. This behavior can be explained by the fact that under constant conditions, when the ozone inlet flow rate is stable, the concentration of dissolved ozone and the produced OH radicals is constant. It should be mentioned that by enhancing PhP concentration, the need for excessive concentration of reactive oxygen species to degrade the molecules of the pharmaceutical increases. However, the concentration of the oxidative species remains constant for a given ozone flow rate and time. Therefore, the amount of the existing oxidative species were not sufficient to degrade the high concentration of PhP. Accordingly, the removal efficiency of PhP decreases as the concentration increases [3].

Additionally, light intensity is a major factor in photocatalytic reactions, because electron–hole pairs are produced by light energy [20,22]. Fig. 4d shows that the pseudo-first order removal rate constant of PhP increases systematically with the light intensity. For example, the degradation rate at 40.05 W/m² is faster than that at 25.22, 22.95 and 15.30 W/m². This is because high light intensity provides high energy for TiO₂ nanoparticles in the thin film to produce electron–hole pairs.

3.4. Reaction mechanism

A heterogeneous photocatalytic ozonation process in a completely mixed semi-batch photoreactor involves several parallel homogeneous and heterogeneous reactions, including homogeneous ozonation, heterogeneous ozonation on the surface of catalyst, homogeneous photolytic-ozonation and heterogeneous photocatalytic ozonation of organic compounds. In the present

work, to simplify the model development, it is assumed that removal of PhP by photocatalytic ozonation process is mainly completed through two major pathways: (i) oxidation by direct and indirect homogeneous ozonation reactions in the solution bulk, its complete mechanism was given in Section 3.4.1 (see Table 2). Accordingly, this oxidation route kinetic was defined as first-order reaction rate expression; (ii) oxidation through heterogeneous photocatalytic ozonation on the surface of immobilized TiO₂ nanoparticles among adsorbed hydroxyl radicals and organic compounds; its complete mechanism was given in Section 3.4.2 (see Table 3). The second oxidation pathway kinetic was described as a second-order surface reaction equation.

3.4.1. Mechanistic aspects of homogeneous ozonation process

The reactivity runs accomplished in ozonation system demonstrated that the majority of PhP oxidation occurred in the presence of ozone and the presence of UV-A irradiation did not influence PhP ozonation degradation rate (Fig. 3a and b). It is well known that in ozonation system direct selective ozone reactions are the first taking place, especially in the case of ozone fast reacting compounds, containing specific functional groups such as double bonds and/or nucleophilic positions [5,10,15]. These reactions lead to the appearance of first intermediates and also, to the formation of free radicals. The free radicals formed eventually give rise to hydroxyl radicals. These free radicals also react with PhP and the produced intermediates. The final result is the development of a mechanism of PhP and organic compounds removal through direct ozone and OH reactions. Also, the appearance of hydrogen peroxide that comes from the aromatic ring opening and double carbon bond breaking is very important in this process. Thus, literature also reports the

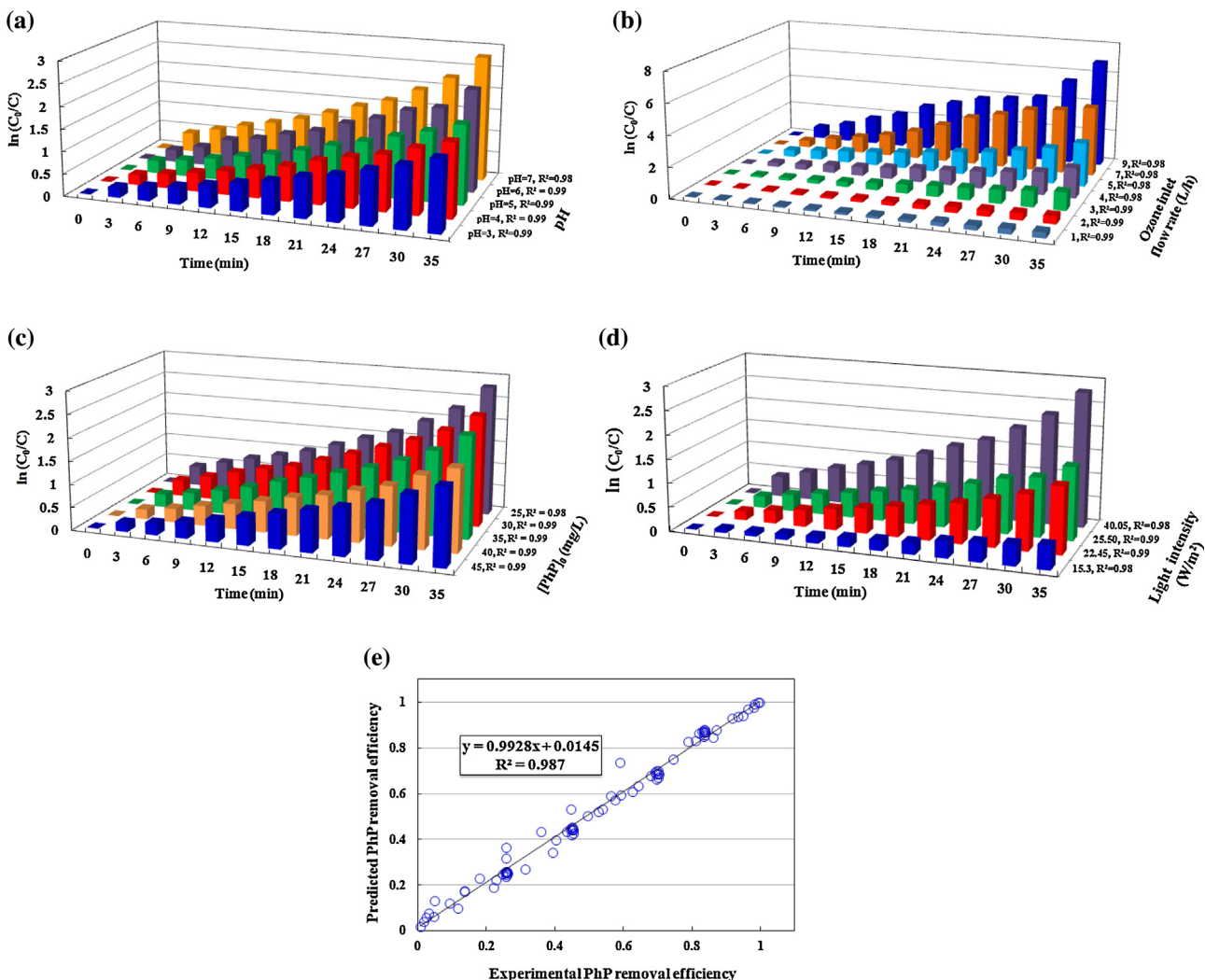


Fig. 4. Linear relationship of PhP degradation during photocatalytic ozonation process at (a) different pH of solution, experimental conditions: [PhP]: 25 mg/L, ozone inlet flow rate: 5 L/h, and light intensity: 40.05 W/m² (b) various ozone inlet flow rates, experimental conditions: [PhP]: 25 mg/L, pH buffered at pH 7 and light intensity: 40.05 W/m²; (c) different initial PhP concentration, experimental conditions: pH buffered at pH 7, ozone inlet flow rate: 5 L/h and light intensity: 40.05 W/m²; (d) different light intensities, experimental conditions: [PhP]: 25 mg/L, pH buffered at pH 7 and zone inlet flow rate: 5 L/h, fitted by the pseudo-first-order model, and (e) comparison of the experimental PhP removal efficiency with those calculated via developed intrinsic kinetic model (Eq. (22)).

Table 2

Reactions involved in oxidation of PhP by homogeneous ozonation process at pH 7.

Reaction No.	Elementary reaction	Kinetic constant	References	
1	$O_3 + PhP \rightarrow$ Degradation products + O_3^- (Direct)			
2	$O_3^- + H^+ \leftrightarrow HO_3^{\cdot}$	$5.2 \times 10^{10} M^{-1} s^{-1}$	$k^- = 3.7 \times 10^4 M^{-1} s^{-1}$	[50,58–61]
3	$HO_3^{\cdot} \rightarrow \cdot OH + O_2$	$5.2 \times 10^{10} M^{-1} s^{-1}$		[50,58–61]
4	$O_3 + \cdot OH \rightarrow HO_2^{\cdot} + O_2$	$70 M^{-1} s^{-1}$		[50,58–61]
5	$O_3 + HO_2^{\cdot} \rightarrow HO_2^{\cdot} + O_3^{\cdot}$	$2.8 \times 10^6 M^{-1} s^{-1}$		[50,58–61]
6	$HO_2^{\cdot} \xleftrightarrow{pk=4.8} O_2^{\cdot\cdot} + H^+$	$3.2 \times 10^5 M^{-1} s^{-1}$	$k^- = 2.0 \times 10^{10} M^{-1} s^{-1}$	[50,58–61]
7	$O_2^{\cdot\cdot} + O_3 \rightarrow O_3^- + O_2$	$1.6 \times 10^9 M^{-1} s^{-1}$		[50,58–61]
8	$2HO_2^{\cdot} \rightarrow O_2 + H_2O_2$	$5.0 \times 10^9 M^{-1} s^{-1}$		[50,58–61]
9	$2HO_3^{\cdot} \rightarrow 2O_2 + H_2O_2$	$5.0 \times 10^9 M^{-1} s^{-1}$		[50,58–61]
10	$\cdot OH + HO_3^{\cdot} \rightarrow O_2 + H_2O_2$	$5.0 \times 10^9 M^{-1} s^{-1}$		[50,58–61]
11	$\cdot OH + PhP \rightarrow IP$ (Indirect)			
12	$\cdot OH + IP \rightarrow DP$			
13	$O_3 + \cdot OH \rightarrow HO_2^{\cdot} + O_2$	$2 \times 10^9 M^{-1} s^{-1}$		[50,58–61]
14	$H_2O_2 + \cdot OH \rightarrow HO_2^{\cdot} + H_2O$	$2.7 \times 10^7 M^{-1} s^{-1}$		[50,58–61]
15	$HO_2^{\cdot} + \cdot OH \rightarrow HO_2^{\cdot} + \cdot OH$	$7.5 \times 10^9 M^{-1} s^{-1}$		[50,58–61]

IP: Refers to intermediate products.

DP: Refers to degradation products.

formation of hydrogen peroxide from direct ozone attack for PhP and other organic compounds with various concentrations [30]. According to these antecedents, reactions 1–15 of Table 2 can be

proposed for homogeneous ozonation of PhP at pH of 7. Reaction 1 of Table 2 shows that the direct reaction of PhP with ozone leads to the formation of ozonide ion radical. Next, the ozonide ion radi-

Table 3

Reactions involved in oxidation of PhP by heterogeneous photocatalytic ozonation process.

Reaction No.	Elementary reaction	Kinetic constant	References
16	$\text{TiO}_2 + h\nu \xrightarrow{\lambda < 365\text{nm}} e^- + h^+$		
17	$e^- + h^+ \rightarrow \text{Heat}$		
18	$\text{TiO}_2 - \text{H}_2\text{O} + h^+ \rightarrow \text{TiO}_2 - \cdot\text{OH}$		
19	$\text{TiO}_2 - \text{OH}^- + h^+ \rightarrow \text{TiO}_2 - \cdot\text{OH}$		
20	$\text{O}_2 + e^- \rightarrow \text{O}_2^-$		
21	$\text{O}_2^- + \text{H}^+ \xrightarrow{pk=4.8} \text{HO}_2^\bullet$	$3.2 \times 10^5 \text{ M}^{-1} \text{ s}^{-1}$	[50,58–61]
22	$2\text{O}_2^- + 2\text{H}^+ \rightarrow \text{H}_2\text{O}_2$	$9.7 \times 10^7 \text{ M}^{-1} \text{ s}^{-1}$	[50,58–61]
23	$2\text{HO}_2^\bullet \rightarrow \text{H}_2\text{O}_2 + \text{O}_2$	$5.0 \times 10^9 \text{ M}^{-1} \text{ s}^{-1}$	[50,58–61]
24	$\text{H}_2\text{O}_2 + e^- \rightarrow \cdot\text{OH} + \text{OH}^-$	$1.1 \times 10^{10} \text{ M}^{-1} \text{ s}^{-1}$	[50,58–61]
25	$\text{TiO}_2 - e^- + \text{O}_3 \rightarrow \text{TiO}_2 - \text{O}_3^\bullet$	$3.6 \times 10^{10} \text{ M}^{-1} \text{ s}^{-1}$	[50,58–61]
26	$\text{TiO}_2 - \text{O}_2^- + \text{O}_3 \rightarrow \text{TiO}_2 - \text{O}_3^\bullet$	$1.6 \times 10^9 \text{ M}^{-1} \text{ s}^{-1}$	[50,58–61]
27	$\text{TiO}_2 - \text{O}_3^\bullet + \text{H}^+ \leftrightarrow \text{HO}_3$	$2.0 \times 10^{10} \text{ M}^{-1} \text{ s}^{-1}$	[50,58–61]
28	$\text{HO}_3 \rightarrow \cdot\text{OH} + \text{O}_2$	$5.0 \times 10^4 \text{ M}^{-1} \text{ s}^{-1}$	[50,58–61]
29	$\text{TiO}_2 - \text{PhP} + \text{TiO}_2 - \cdot\text{OH}_{\text{ads}} \rightarrow \text{IP}$		
30	$\text{TiO}_2 - \text{IP} + \text{TiO}_2 - \cdot\text{OH}_{\text{ads}} \rightarrow \text{DP}$		

IP: Refers to intermediate products.

DP: Refers to degradation products.

cal triggers a free radical mechanism leading to the appearance of hydroxyl free radicals (reaction 2 and 3): Hydroxyl radicals are also formed from the reactions of ozone with hydroxyl ions and hydrogen peroxide ionic form reactions 4 and 5. At pH 7 reaction 6 is shifted to the right so that the hydroperoxide radical (HO_2^\bullet) converts to a superoxide ion radical ($\text{O}_2^\bullet^-$). This is very important when ozone is also present since the superoxide ion radical reacts very fast with ozone yielding more hydroxyl radicals through reactions 7, 2 and 3. Hydroxyl free radicals start to react with PhP, intermediates, ozone and hydrogen peroxide to yield more intermediates, free radicals and so on (reactions 10 to 15).

3.4.2. Mechanistic aspects of heterogeneous photocatalytic ozonation process

The main steps of photocatalytic process are presented in reaction 16–29 of Table 3 [10,22,31]. The first step is the absorption of light by the semiconductor which leads to the formation of h^+ on the valence band and migration of e^- to the conduction band. Reactions 18 and 19 show adsorption of water on activated points of TiO_2 nanoparticles and formation of OH from h^+ oxidation. In the presence of oxygen electrons can be trapped by oxygen in the conduction band to prevent electron-hole recombination and process suppression (reaction 20). Also, adsorbed superoxide ion radicals can react with the organic matter, or be recombined to yield hydrogen peroxide, where hydrogen peroxide can also be adsorbed (reactions 20–24). Besides, $\cdot\text{OH}$ can be formed from hydrogen peroxide oxidation on the surface of the semiconductor. Contribution of these reactions, however, can be neglected when ozone is present. Thus, reaction 24 seems to be of low probability since the produced electrons on the surface of the semiconductor likely reacts with ozone because of its high powerful oxidant character. In the presence of TiO_2 and UV-A light, ozone molecules can be absorbed on the surface of the illuminated photocatalyst and hence participate in the surface redox reactions as a trap for the electron–hole pairs as generated in the photoexcitation process (reactions 25 to 28). Reactions 25–28 indicate both the strong electrophilic property of ozone which leads to the formation of $\text{O}_3^\bullet^-$ and its participation in the surface redox reaction which brings about various ROS such as $\cdot\text{OH}$. The mechanism shown in reactions 25 to 28 demonstrates a synergistic effect between ozone and TiO_2 nanocatalyst under UV-A irradiation. Thus, the advantages of using the integrated photocatalytic ozonation process are not only attributed to the sum of individual processes but also to the synergistic effect which consequently reduces the recombination of electrons and holes through reaction 25. It leads to the formation of high amounts of oxidizing species. This phenomenon has

been reported for the photocatalytic ozonation of different organic pollutants in water [12,24].

3.5. Model development based on intrinsic elementary reactions

The main reaction steps which participate in the heterogeneous photocatalytic ozonation of PhP on the surface of TiO_2 under UV-A radiation are illustrated in Table 3. The mentioned mechanism of reactions can be simplified depending on the experimental conditions and nature of the compounds treated. For example, in the present work it is assumed that ozone preferentially reacts with the produced electron on the surface of TiO_2 because of its high oxidation character. This leads to the production of adsorbed ozonide ion radicals that eventually result in more active radicals (reactions 25–28). Reactions 20 and 24 are negligible in comparison with reaction 25. However, reaction 20 was not neglected due to the high concentration of dissolved oxygen in the solution bulk under the applied ozone inlet flow rate. Also, the production of $\text{O}_2^\bullet^-$ form reaction 21 is neglected due to the applied pH conditions (pH of 7). Moreover, the recombination of reactive oxygen species with each other seems to be of low probability due to the presence of organic compound, so reactions 22 and 23 are neglected. Based on the above-mentioned explanations, the PhP degradation rate expression is derived from the following assumptions:

- the steady state approximation (SSA) is used for calculating the concentration of unstable reaction species such as radicals and e^- and h^+ on TiO_2 surface;
- the concentrations of e^- and h^+ are equal;
- the concentrations of water and hydroxide ions on TiO_2 surface are approximately constant,
- equilibrium conditions are obtained between the adsorbed and bulk concentrations of PhP;
- there is a competitive adsorption mechanism between PhP and its degradation intermediates;
- the adsorption of oxygen and ozone on TiO_2 surface sites does not compete with PhP and its degradation intermediates;

The overall reaction rate expression for pseudo-first-order homogeneous reaction and second-order surface reaction of PhP can be written as Eq. (2):

$$r_{\text{Tot}} = -\frac{1}{V} \frac{dN}{dt} = -\frac{dC}{dt} = k_{\text{homo}}[\text{PhP}] + k_{\text{hetero}}[\cdot\text{OH}]_{\text{ads}}[\text{PhP}] \quad (2)$$

where r_{Tot} is the total reaction rate, V is the reaction volume, N is the PhP moles, t is the reaction time, C is the concentration of

Table 4

Values of the constants for equations 20 and 21 obtained from least square curve fit method.

Developed model	Constant	Value	R^2	SSE	RMSE
$k_{app(LCofe-anth^+)} = \frac{\alpha_1 + \beta_1 I + \eta_1 I [O_3] + \lambda_1 I [O_2]}{\lambda_1 [PhP]_0}$	α_1	0.0595 (± 0.0256)			
	β_1	0.1302 (± 0.0958)			
	η_1	0.3697 (± 0.0992)			
	λ_1	1.8790 (± 0.7892)			
	γ_1	1.5745 (± 0.5672)			
$k_{app(HCofe-anth^+)} = \frac{\alpha_2 + \beta_2 I^{1/2} + \eta_2 I^{1/2} [O_3] + \lambda_2 I^{1/2} [O_2]}{\lambda_2 [PhP]_0}$	α_2	0.0619 (± 0.0312)	0.995	4.2764×10^{-4}	0.0103
	β_2	0.0231 (± 0.0357)			
	η_2	0.0991 (± 0.0066)			
	λ_2	0.9648 (± 0.3529)			
	γ_2	1.1664 (± 0.4125)			

PhP at time t , k_{homo} is the first-order rate constant of the homogeneous ozonation in the liquid phase, and k_{hetero} is the second-order kinetic constant of the photocatalytic ozonation reaction between adsorbed hydroxyl radicals ($[^\bullet OH]_{ads}$) and PhP molecules ($[PhP]$).

By considering the SSA for total concentration of adsorbed hydroxyl radicals, the expression for $[^\bullet OH]_{ads}$ can be achieved by Eq. (3).

$$\frac{d[^\bullet OH]}{dt} = k_{18}[H_2O]_{ads}[h^+] + k_{19}[OH^-]_{ads}[h^+] + k_{28}[HO_3^\bullet]_{ads} - k_{29}[PhP]_{ads}[^\bullet OH]_{ads} - k_{30}[IP]_{ads}[^\bullet OH]_{ads} \approx 0 \quad (3)$$

By considering the fact that the experiments have been performed in pH of 7 and water is solvent ($k_{18}[H_2O]_{ads}[h^+] \gg k_{19}[OH^-][h^+]$) and its concentration is constant ($k_{18}[H_2O] = k'_{18}$), it can be assumed that hydroxyl radicals are mainly formed via reaction 18 (trapping the holes by adsorbed water molecules) and reaction 28. So, Eq. (3) is rearranged as Eq. (4):

$$[^\bullet OH]_{ads} = \frac{k'_{18}[h^+] + k_{28}[HO_3^\bullet]}{k_{29}[PhP]_{ads} + k_{30}[IP]_{ads}} \quad (4)$$

It should be stated that in Eq. (4) the concentration of $[PhP]_{ads}$ and $[IP]_{ads}$ are somehow difficult to measure, but, by considering the assumption presented in Eqs. (5) and (4) can be modified to Eq. (6). In fact, Eq. (5) demonstrates the assumption in which the term $k_{29}[IP] - k_{30}[PhP]_{ads}$ is much lower than $(k_{29} + k_{30})[PhP]_0$, so it can be neglected [22].

$$[PhP]_{ads} + [IP] = [PhP]_0$$

$$\Rightarrow k_{29}[PhP]_{ads} + k_{30}[IP]_{ads} = k_{29}([PhP]_0 - [IP]) + k_{30}([PhP]_0 - [PhP]_{ads}) = \quad (5)$$

$$(k_{29} + k_{30})[PhP]_0 - k_{29}[IP] - k_{30}[PhP]_{ads} \approx (k_{29} + k_{30})[PhP]_0$$

By substituting Eq. (5) in Eq. (4), Eq. (6) is obtained.

$$[^\bullet OH]_{ads} = \frac{k'_{18}[h^+] + k_{28}[HO_3^\bullet]}{(k_{29} + k_{30})[PhP]_0} \quad (6)$$

The concentration of photogenerated holes, h^+ , can be obtained by using the SSA which was presented in Eq. (7):

$$\frac{d[h^+]}{dt} = k_{16}[TiO_2]I - k_{17}[h^+]^2 - k_{18}[H_2O]_{ads}[h^+] - k_{19}[OH^-]_{ads}[h^+] \approx 0 \quad (7)$$

By considering $k_{18}[H_2O]_{ads}[h^+] \gg k_{19}[OH^-][h^+]$, and regarding that the concentration of the catalyst and water were constant during all of the experiments ($k_{16}[TiO_2]I = k'_{16}I$ and $k_{18}[H_2O]_{ads}[h^+] = k_{18}'[h^+]$) Eq. (7) transformed to Eq. (8).

$$k'_{16}I = k_{17}[h^+]^2 + k'_{18}[h^+] \quad (8)$$

However, Eq. (8) can be transformed to two different equations according to the two different assumptions which were made in literature for concentration of h^+ as follows:

(i) The trapping of h^+ with water molecules can compete with recombination reaction [22,32,33]. In other words, the kinetic model for degradation is developed by taking in to account that $k_{17}[h^+]^2 \ll k'_{18}[h^+]$. Subsequently, Eq. (9) is considered as an expression for h^+ concentration.

$$[h^+] = \left(\frac{k'_{16}}{k'_{18}} \right) I \quad (9)$$

(ii) The recombination rate coefficient of the separated e^- and h^+ is much higher than trapping of h^+ by water molecules [22,34,35]. So, the kinetic model for degradation is proposed by considering that $k_{17}[h^+]^2 >> k'_{18}[h^+]$ and the expression for h^+ concentration can be achieved from Eq. (10).

$$[h^+] = \left(\frac{k'_{16}}{k_{17}} \right)^{1/2} I^{1/2} \quad (10)$$

Ollis et al. [36] described the transformation of the order one of the h^+ concentration with regard to the intensity to an order of 1/2 which could be explained by the recombination of the electron-hole. According to Rothenberger et al. [34] below a given light intensity in which the concentration of separated e^- and h^+ is low, trapping of holes with water molecules can compete with e^- and h^+ recombination (Eq. (9)) and above this value in which the concentration of e^- and h^+ is high the trapping is a much slower process and the recombination becomes limiting (Eq. (10)). Herein we developed two kinetic models considering assumptions (I) and (II) and the two obtained Eqs. (9) and (10) and then, the fitting of two models with experimental results was compared.

Also, by applying the SSA for the concentration of hydrogen trioxy radical (HO_3^\bullet), superoxide ion radicals ($O_2^\bullet-$), and $O_3^\bullet-$ and considering all the assumptions described on Section 3.5 Eqs. (11)–(13) could be achieved:

$$\frac{d[HO_3^\bullet]}{dt} = k'_{27}[O_3^\bullet] - k_{28}[HO_3^\bullet] \approx 0 \Rightarrow [HO_3^\bullet] = \frac{k'_{27}[O_3^\bullet]}{k_{28}} \quad (11)$$

$$\frac{\frac{d[O_3^\bullet]}{dt}}{k_{25}[e^-][O_3] + k_{26}[O_2^\bullet][O_3]} = \frac{k_{25}[e^-][O_3] + k_{26}[O_2^\bullet][O_3]}{k'_{27}} \quad (12)$$

$$\frac{d[O_2^\bullet]}{dt} = k_{20}[e^-][O_2] - k_{26}[O_2^\bullet][O_3] \approx 0 \Rightarrow [O_2^\bullet] = \frac{k_{20}[e^-][O_2]}{k_{26}[O_3]} \quad (13)$$

By placing of Eqs. (13) and (12) into Eqs. (12) and (11), respectively the expression for the HO_3^\bullet concentration is obtained from Eq. (14):

$$[HO_3^\bullet] = \frac{k_{25}[e^-][O_3] + k_{20}[e^-][O_2]}{k_{28}} \quad (14)$$

Now, by substituting Eq. (14) into Eq. (6), Eq. (15) can be represented for the concentration of adsorbed •OH radicals.

$$[\text{•OH}_{\text{ads}}] = \frac{k'_{18}[\text{h}^+] + k_{25}[\text{e}^-][\text{O}_3] + k_{20}[\text{e}^-][\text{O}_2]}{(k_{29} + k_{30})[\text{PhP}]_0} \quad (15)$$

In this step, by substituting each of Eqs. (9) and (10) into Eq. (15) separately, and combining the concentration of adsorbed hydroxyl radicals with Eq. (2), the expressions for the total degradation rate equation of PhP can be described by Eqs. (16) and (17) regarding assumption (I) (low concentration of e⁻ and h⁺ (LC of e⁻ and h⁺)) and assumption (II) (high concentration of e⁻ and h⁺ (HC of e⁻ and h⁺)), respectively.

$$r_{\text{Tot(LCofe}^- \text{andh}^+)} = k_{\text{homo}}[\text{PhP}] + \frac{k_{\text{hetro}} \left\{ k'_{18} \left(\frac{k'_{16}}{k'_{18}} \right) I + k_{25} \left(\frac{k'_{16}}{k'_{18}} \right) I[\text{O}_3] + k_{20} \left(\frac{k'_{16}}{k'_{18}} \right) I[\text{O}_2] \right\}}{(k_{29} + k_{30})[\text{PhP}]_0} [\text{PhP}] \quad (16)$$

$$r_{\text{Tot(HCofe}^- \text{andh}^+)} = k_{\text{homo}}[\text{PhP}] + \frac{k_{\text{hetro}} \left\{ k'_{18} \left(\frac{k'_{16}}{k'_{17}} \right)^{1/2} I^{1/2} + k_{25} \left(\frac{k'_{16}}{k'_{17}} \right)^{1/2} I^{1/2}[\text{O}_3] + k_{20} \left(\frac{k'_{16}}{k'_{17}} \right)^{1/2} I^{1/2}[\text{O}_2] \right\}}{(k_{29} + k_{30})[\text{PhP}]_0} [\text{PhP}] \quad (17)$$

Eqs. (16) and (17) can be transformed to a pseudo-first-order rate equation, (Eq. (1)), if Eqs. (18) and (19) are considered as a pseudo-first-order rate constant, respectively.

$$k_{\text{app(LCofe}^- \text{andh}^+)} = k_{\text{homo}} + \frac{k_{\text{hetro}} k'_{18} \left(\frac{k'_{16}}{k'_{18}} \right) I + k_{\text{hetro}} k_{25} \left(\frac{k'_{16}}{k'_{18}} \right) I[\text{O}_3] + k_{\text{hetro}} k_{20} \left(\frac{k'_{16}}{k'_{18}} \right) I[\text{O}_2]}{(k_{29} + k_{30})[\text{PhP}]_0} \quad (18)$$

$$k_{\text{app(HC of e}^- \text{and h}^+)} = k_{\text{homo}} + \frac{k_{\text{hetero}} k'_{18} \left(\frac{k'_{16}}{k'_{17}} \right)^{1/2} I^{1/2} + k_{\text{hetero}} k_{25} \left(\frac{k'_{16}}{k'_{17}} \right)^{1/2} I^{1/2}[\text{O}_3] + k_{\text{hetero}} k_{20} \left(\frac{k'_{16}}{k'_{17}} \right)^{1/2} I^{1/2}[\text{O}_2]}{(k_{29} + k_{30})[\text{PhP}]_0} \quad (19)$$

Eqs. (18) and (19) can be simplified to Eqs. (20) and (21) by considering $\alpha_1 = k_{\text{homo}}$, $\beta_1 = k_{\text{hetero}} k'_{18} \left(\frac{k'_{16}}{k'_{18}} \right)$, $\eta_1 = k_{\text{hetero}} k_{25} \left(\frac{k'_{16}}{k'_{18}} \right)$, $\lambda_1 = k_{\text{hetero}} k_{20} \left(\frac{k'_{16}}{k'_{18}} \right)$, $\gamma_1 = k_{29} + k_{30}$ and $\alpha_2 = k_{\text{homo}}$, $\beta_2 = k_{\text{hetero}} k'_{18} \left(\frac{k'_{16}}{k'_{17}} \right)^{1/2}$, $\eta_2 = k_{\text{hetero}} k_{25} \left(\frac{k'_{16}}{k'_{17}} \right)^{1/2}$, $\lambda_2 = k_{\text{hetero}} k_{20} \left(\frac{k'_{16}}{k'_{17}} \right)^{1/2}$ and $\gamma_2 = k_{29} + k_{30}$, as the equation constants of Eqs. (18) and (19), respectively.

$$k_{\text{app(LCofe}^- \text{andh}^+)} = \alpha_1 + \frac{\beta_1 I + \eta_1 I[\text{O}_3] + \lambda_1 I[\text{O}_2]}{\lambda_1 [\text{PhP}]_0} \quad (20)$$

$$k_{\text{app(HCofe}^- \text{andh}^+)} = \alpha_2 + \frac{\beta_2 I^{1/2} + \eta_2 I^{1/2}[\text{O}_3] + \lambda_2 I^{1/2}[\text{O}_2]}{\lambda_2 [\text{PhP}]_0} \quad (21)$$

Eqs. (20) and (21) can be used to explain the interdependence of pseudo-first-order kinetic constant with regard to the light intensity, ozone dissolved concentration, oxygen dissolved concentration and initial PhP concentration. The equations constants α_1 , β_1 , η_1 , λ_1 , γ_1 and α_2 , β_2 , η_2 , λ_2 and γ_2 were calculated for the given dissolved ozone, oxygen concentrations initial PhP concentration and light intensity using a least square curve fit method by Matlab 7.11 software and are given in Table 4. To compare the experimental and calculated apparent rate constants, the correlation coefficient (R^2) values, sum of squared error (SSE) and root-mean-square error (RMSE) were obtained as the performance error functions. According to the results given in Table 4, the values of k_{app} calculated using Eq. (21) by considering assumption (II) (high concentration of e⁻ and h⁺ (HC of e⁻ and h⁺)) are in good agreement with experimental k_{app} . Ultimately, by combining Eqs. (1) and (21), expression for predicting PhP removal efficiency (RE) related to the operational parameters can be defined as Eq. (22).

$$\text{RE}_{\text{predicted(HCofe}^- \text{andh}^+)} = 1 - \exp \left(- (0.0619 + \frac{0.0231 I^{1/2} + 0.0991 I^{1/2}[\text{O}_3] + 0.9648 I^{1/2}[\text{O}_2]}{1.1664 [\text{PhP}]_0}) \times t \right) \quad (22)$$

Table 5

Values of the constants for equation 24 obtained from nonlinear fitting of experimental data.

Parameter	Range	μ	θ	R^2
pH	3–7	0.019	0.654	0.955
Ozone inlet flow rate (L/h)	1–9	0.007	1.418	0.963
Initial PhP concentration (mg/L)	25–45	0.929	-0.789	0.972
Light intensity (W/m ²)	15.30–40.05	0.0002	1.639	0.974

For experimental conditions related to Fig. 5a-d.

To assess the performance of the developed kinetic model the diagram of dispersion of the predicted PhP removal efficiency, calculated from Eq. (22), versus experimental PhP removal efficiency

is presented in Fig. 4e. A test of the significance of the correlation coefficient (R^2) was performed on the data of Fig. 4e. The value of 0.987 for R^2 indicates that there is a significant correlation between the experimental PhP removal efficiency and the fitted model based on Eq. (22). The value of R^2 is an obvious proof that the correlation is valid and corroborates the interdependence of the pseudo-first-order rate constant with respect to light intensity, initial PhP concentration, dissolved ozone and dissolved oxygen concentrations. The excellent fit obtained for the photocatalytic ozonation of PhP, distinctly signifies that this form of model describes more closely the real trend and mechanism of the photocatalytic ozonation process. It can be concluded that the proposed reaction mechanism and the applied assumptions through the modeling process is valid (see Sections 3.4 and 3.5). In order to further evaluate the efficiency of the developed model (Eq. (22)) the process is modeled with empirical modeling based on nonlinear regression analysis and ANN in the following sections.

3.6. Development of empirical model based on nonlinear regression analysis

By examining the obtained experimental results demonstrated in Section 3.1, it can be inferred that photocatalytic ozonation of PhP followed pseudo-first-order kinetic. Also, from Fig. 4a-d it can be seen that the pseudo-first-order rate constant, k_{app} , is a function of pH, ozone inlet flow rate and initial PhP concentration. In the simplest case, the relationship between k_{app} and each of the above-mentioned parameters, X, can be modeled with a non-linear relation such as the empirical power law-type which is described

by Eq. (23).

$$k_{\text{app}} = \mu_i(X_i)^{\theta_i} \Rightarrow \mu_{ia}(X_1)^{\theta_1} \times (X_2)^{\theta_2} \times \dots \times (X_n)^{\theta_n} \quad (23)$$

where μ_i and θ_i are the model parameters and μ_{ia} is the average of the calculated μ_i values. The model constants were calculated for each operational parameter (X) with non-linear regression analysis of series of experimental data by Matlab 7.11 software and the obtained results are shown in Fig. 5a-d and Table 5. Fig. 5a-d illustrate that k_{app} can be empirically correlated to the effect of operating parameters such as pH, ozone inlet flow rate PhP initial concentration and light intensity, respectively. By substituting the obtained constant values given in Table 5 into Eq. (23), the expression for predicting k_{app} at various experimental conditions can be obtained from Eq. (24) as follows:

$$k_{\text{app}} = 4.880 \times 10^{-5} [\text{pH}]^{0.654} [\text{ozoneinletflowrate}]^{1.418} [\text{PhP}]^{-0.789} [\text{Lightintensity}]^{1.639} \quad (24)$$

Consequently, an empirical kinetic expression for calculating PhP removal efficiency by the photocatalytic ozonation process is represented as Eq. (25) which is developed by incorporating Eqs. (1) and (24).

$$\begin{aligned} \text{RE}_{\text{predicted}} &= 1 - \exp(-4.88 \times 10^{-5} [\text{pH}]^{0.654} \\ &[\text{ozoneinletflowrate}]^{1.418} [\text{PhP}]^{-0.789} [\text{Lightintensity}]^{1.639} \times t) \end{aligned} \quad (25)$$

A comparison between experimental and predicted PhP removal efficiencies, which is calculated from the mathematical empirical model (Eq. (25)), is demonstrated in Fig. 5e. It can be observed that the calculated RE are in good consistent with the experimental data ($R^2 = 0.982$). So, it can be proposed that empirical modeling of the process based on nonlinear regression analysis is a simple method of modeling, which accurately defines the interdependence kinetic rate constant to the main operational parameters. However, in the present work the performance of the developed models is exactly and precisely evaluated on Section 3.8.

3.7. Artificial neural network modeling of the photocatalytic ozonation process

An ANN is a mathematical algorithm that can develop a relation between independent and dependent parameters of a process, allowing us to investigate and model the effect of the operational parameters on the final response of a system under different operating conditions. The mathematical relationship among the output and input parameters is given in Eqs. (26) and (27) [37].

$$D_t = \sum_{i=1}^M W_{ti} X_i \quad (26)$$

$$Y_t = \phi(D_t + B_t) \quad (27)$$

where X_1, \dots, X_M are the input data, W_{t1}, \dots, W_{tM} are the weights of neuron t , D_t is the linear combiner output due to the input data, B_t is the bias, ϕ is the transfer function and Y_t is the output data from the neuron.

In this context, first a relation between operational variables and the response variable is established by an ANN. Then, this relationship or ANN model can be used for predicting the response variable under different operational conditions (modeling section). In this section, modeling of a photocatalytic ozonation process using an ANN has been demonstrated. The samples were divided

into training, validation and test subsets of 128, 28 and 28 samples, respectively. The validation and test sets were randomly selected from the experimental data to evaluate the validating and modeling ability of the model. Pre-processing of the input data was performed by normalizing them in the range of -1 to 1, since the used transfer function in the hidden layer was tangent sigmoid. Using this procedure, all the data (Y_i), containing the training, validation and test sets were scaled to a new value Y_{norm} using Eq. (28) [38].

$$Y_{\text{norm}} = 0.6 \left(\frac{Y_i - Y_{i,\min}}{Y_{i,\max} - Y_{i,\min}} \right) + 0.2 \quad (28)$$

where $Y_{i,\min}$ and $Y_{i,\max}$ are the extreme values of variable Y_i . It should be mentioned that the target data were not normalized to a new scale because a purely linear transfer function was utilized to connect the hidden layer to the output layer.

3.7.1. Selection of the optimal ANN topology

An ANN configuration (topology) is composed of several layers of processing units that are termed neurons, nodes and transfer functions [39]. The input data are processed through these neurons and transfer functions and are sent to the neurons in the hidden layer. The connections between the input, hidden and output neurons have a related parameter indicating the strength of these connections, termed weight, defined in Eq. (26). An important step in development of an ANN model is the optimization of its configuration. In this work, a three-layered feed forward back propagation neural network (5:14:1) was applied to model PhP removal efficiency by the photocatalytic ozonation process for the first time.

The train scaled conjugate gradient 'trainscg', hyperbolic tangent sigmoid 'tansig' and a purely linear transfer function 'purelin' was selected as training, the input to hidden layer and the hidden layer to the output layer transfer functions, respectively. The relations of the aforementioned transfer functions are given in Eqs. (29)–(31). Other activation functions can also be applied such as linear and quadratic, each with a diversity of modeling applications [37].

$$\text{Logsig}(x) = \frac{1}{1 + \exp(-x)} \quad (29)$$

$$\text{Transig}(x) = \frac{2}{1 + \exp(-2x)} - 1 \quad (30)$$

$$\text{Purelin}(x) = x \quad (31)$$

So, it can be concluded that ANN model perform a non-linear functional assessment from previous observation to the future values (Y_t) as described in Eq. (32) [37,40].

$$Y_t = f(X_i, W_{ti}) + B_t \quad (32)$$

Fig. 6a shows a typical ANN with four neurons in the input layer, ten neurons in the hidden layer and one neuron in the output layer with their related transfer functions. The input variables to the feed forward neural network were initial pH, ozone inlet flow rate (L/h), initial PhP concentration (mg/L), reaction time (min) and light intensity. PhP removal efficiency was selected as the output variable or response parameter.

The range of investigated variables is given in Table 6. In order to specify the optimum number of hidden neurons, a series of configurations were used, in which the number of nodes was altered from 2 to 20. Different types of functions were employed to determine and compare the performance of the ANN for the various configurations, namely the mean relative error (MRE), standard deviation in relative errors (STDR), mean squared error (MSE), mean absolute error (MAE) and standard deviation in absolute error (STDA).

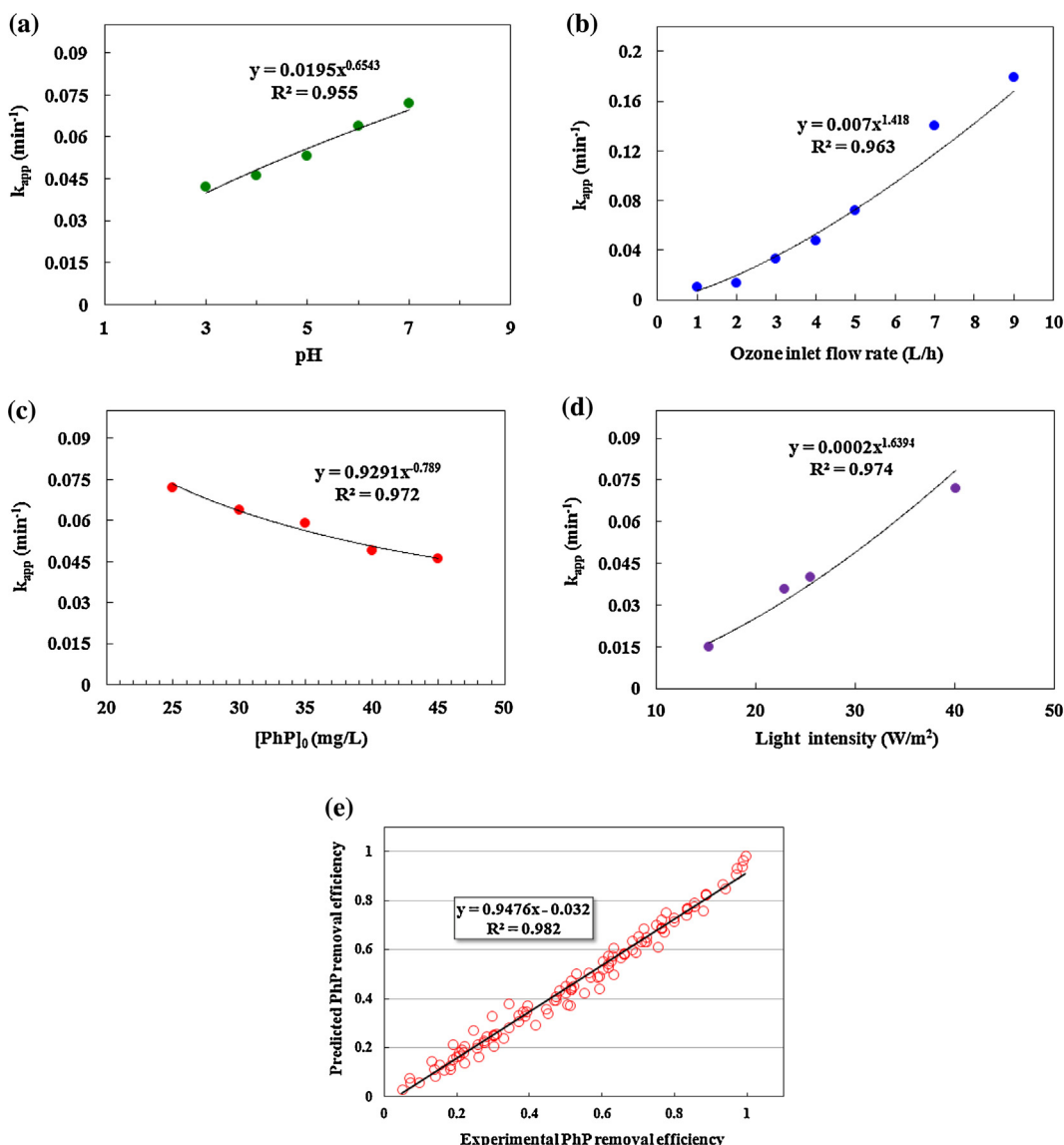


Fig. 5. The effect of (a) pH; (b) ozone inlet flow rate (c) initial PhP concentration and (d) light intensity on pseudo-first-order kinetic constant (k_{app}) and (e) comparison of the experimental PhP removal efficiency with those calculated via developed empirical kinetic model (Eq. (25)). For experimental details refer to Table 5.

Table 6
ANN model variables and their ranges.

Variable	Range
Input layer	
pH	3–7
Ozone inlet flow rate (L/h)	1–9
Initial PhP concentration (mg/L)	25–45
Light intensity (W/m ²)	15.30–40.05
Reaction time (min)	0–35
Output layer	
PhP removal efficiency (%)	0–100

In the present work, the optimum configuration of the ANN model and its parameters were specified based on the minimum value of the MSE of the training and validation sets. MSE calculates performance of network as defined in Eq. (33) [37,41].

$$MSE = \frac{\sum_{i=1}^M (Y_{i,pred} - Y_{i,exp})^2}{M} \quad (33)$$

where M is the number of target data, and $Y_{i,pred}$ and $Y_{i,exp}$ are the network prediction and the experimental response and i is the index of data.

In addition, a number of training runs were done to look out for the best possible weights in error back propagation framework and the final selected network architecture was trained for 6 iterations. As shown in Fig. S1 of Supporting information, the value of MSE is minimum for the train, validation and test data at 6 iterations. Also, from Fig. S2 of supporting information the error histogram for these data series can be observed. Fig. 6b depicts the relationship between network error and number of neurons in the hidden layer for the train, validation and test data. As can be seen in Fig. 6b, the MSE is minimum at about 14 neurons for the train, validation and test data. Hence, a network with 14 neurons in hidden layer is selected as the best topology for modeling approach in best behavior without over-fitting.

To calculate the train, validation and test errors, all outputs were returned to their original scale and then compared with the experimental values. Fig. 7a-d show the comparison between the calculated and experimental values of the output variable for the train, validation, test and all the data sets. As can be seen from

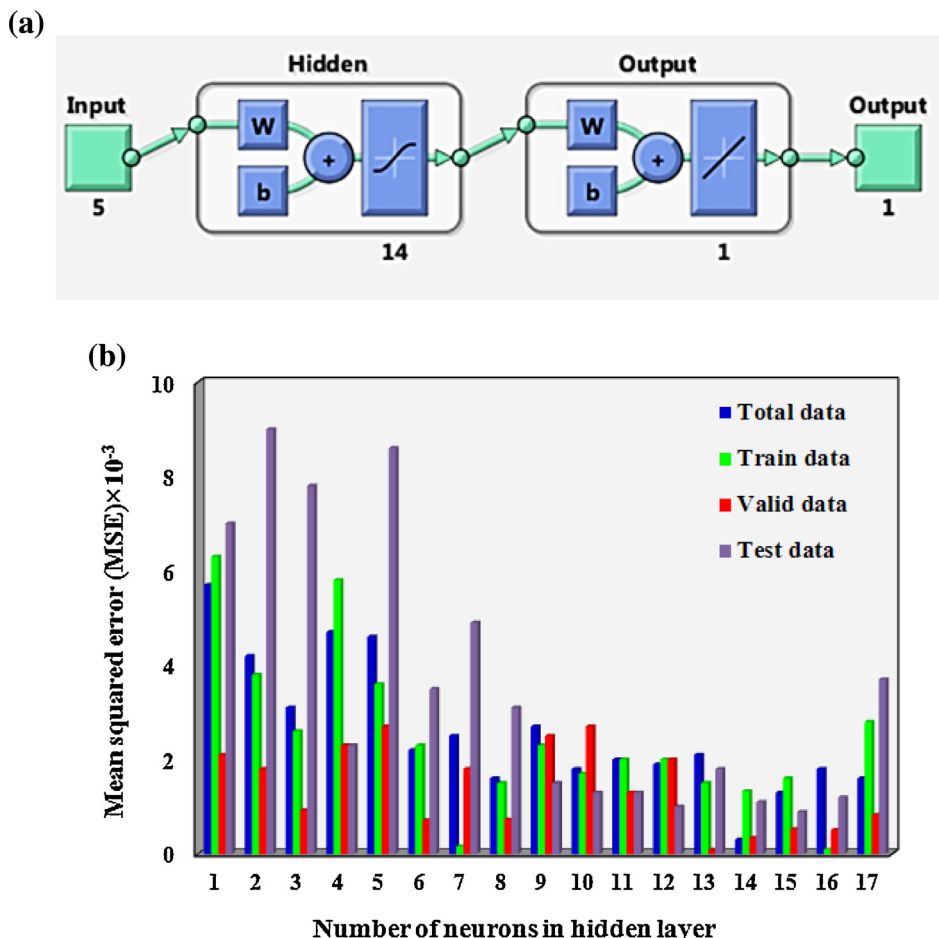


Fig. 6. (a) The schematic of ANN optimized topology and (b) mean squared errors in the prediction of PhP removal efficiency (%) with different number of neurons in the hidden layer for train, validation and test data sets.

the data in Fig. 7, the R^2 values of the plots are 0.991, 0.988, 0.995 and 0.993 for the train, validation, test and all of the data, respectively. A high R^2 value demonstrates that there is a small difference between the experimental and predicted values of the output variable for various subsets. It also confirms that the developed topology (5:14:1) predicts adequately the PhP removal efficiency and possesses suitable generalization ability. This generalization ability is very important to predict the performance of the process under various operational conditions.

3.8. Comparison of developed intrinsic kinetic, empirical kinetic and ANN models

The performance of the developed intrinsic kinetic, empirical kinetic and ANN models for predicting the PhP removal efficiency under different operating conditions was assessed and compared using MSE, mean absolute error (MAE) as the error functions and R^2 . The values of MSE and MAE functions are calculated using Eqs. (33) and (34), respectively [39].

$$MAE = \left(\frac{1}{M} \sum_{i=1}^M |Y_{i,pred} - Y_{i,exp}| \right) \quad (34)$$

where M is the number of target data, and $Y_{i,pred}$ and $Y_{i,exp}$ are the model prediction and the experimental response and i is the index of data.

The values of MSE, MAE and R^2 are presented in Table 7. The achieved R^2 values using the developed models indicates that

intrinsic kinetic, empirical kinetic and ANN models can describe 98.7%, 98.2% and 99.3% variability in PhP removal efficiency, respectively. As a consequence, it can be inferred that only 1.3%, 1.8% and 0.7% of variations in the response is not supported by the intrinsic kinetic, empirical kinetic and ANN models, respectively. The ANN model shows larger deviation compared to the other two models. However, in order to deeply probe and compare the performances of the developed models, analysis of variance was done and the attained results are presented in Table 8. The results from ANOVA explicitly shows that there is no significant difference ($F_{ratio} \ll F_{critical}$) among the predicted PhP removal efficiency by the three proposed models. This fact confirms two main topics. Firstly, this verifies that the intrinsic kinetic model has been developed based on the accurate elementary reactions involved in the heterogeneous photocatalytic ozonation process (see Section 3.5). To state the fact differently, the acceptable prediction capability of the intrinsic kinetic model (no significant difference with empirical and ANN prediction capability) corroborates that the assumptions made during model development was valid. Secondly, it demonstrates that the complex process such as heterogeneous photocatalytic ozonation process can be modeled by the three types of the models introduced. Also, it should be stated that each of the models established in the present work have some related advantages and disadvantages. So, they can be selected regarding the operating conditions of the system and their benefits. As an example, the kinetic model based on the elementary reactions constitutes an intrinsic kinetic description of the heterogeneous photocatalytic ozonation reaction. Therefore, it can be utilized in a

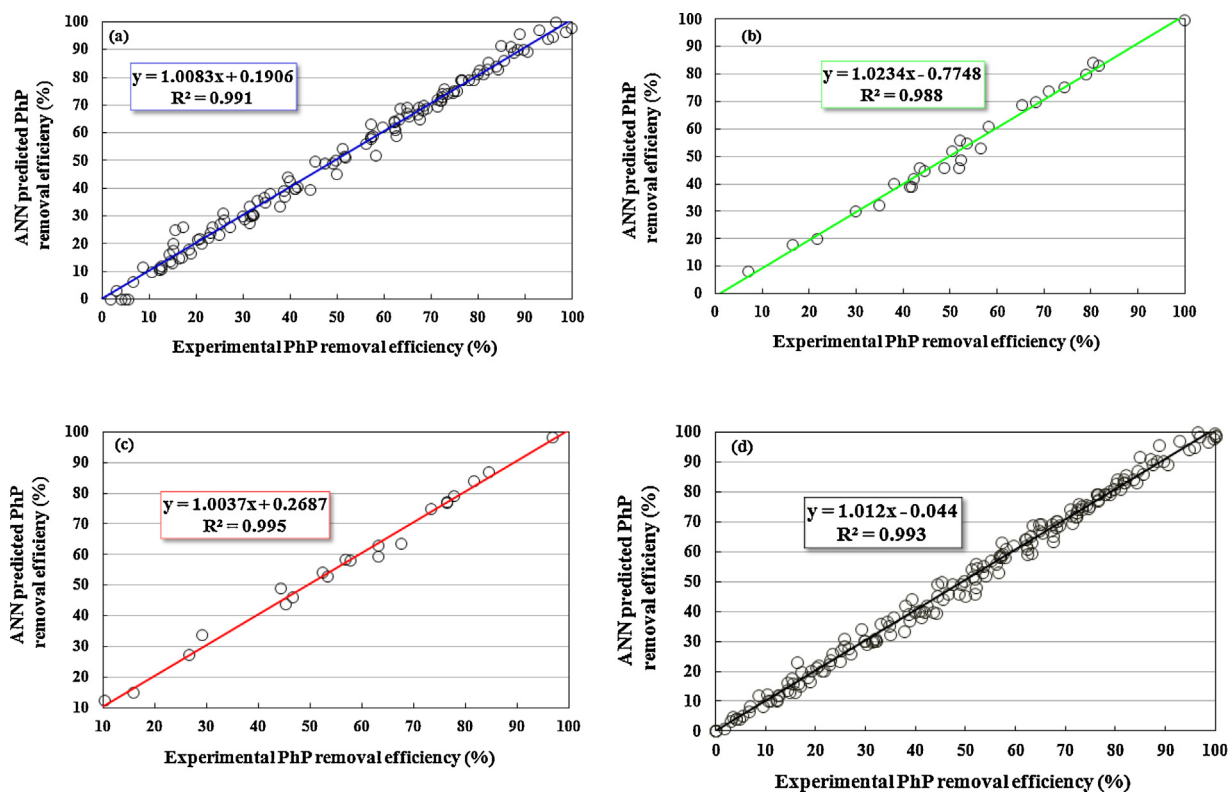


Fig. 7. Regression plots for comparison of the experimental PhP removal efficiency with those calculated via neural network modeling using four input variables, ten processing elements in hidden layer and one output variable (5:14:1) for the (a) train set; (b) validation set; (c) test set and (d) all data set.

Table 7
Comparison between performances of the developed models.

Developed model	$RE_{predicted}$	R^2	MSE	MAE
Intrinsic kinetic model	$RE_{predicted(HCofe-andh^+)} = 1 - \exp\left(-\left(0.0619 + \frac{0.0231I^{1/2} + 0.0991I^{1/2}[O_3] + 0.9648I^{1/2}[O_2]}{1.1664[PhP]_0}\right) \times t\right)$	0.987	0.0011	0.029
Empirical kinetic model	$RE_{predicted} = 1 - \exp(-4.88 \times 10^{-5}[pH]^{0.654}[ozoneinletflowrate]^{1.418}[PhP]^{-0.789}[Lightintensity]^{1.639} \times t)$	0.982	0.005	0.064
Artificial neural network	A three-layered feed forward back propagation neural network with 5:10:1 topology	0.993	5.0265	1.7114

R^2 : Correlation coefficient.

MSE: Mean squared error.

MAE: Mean absolute error.

Table 8
ANOVA analysis for assessing differences among the predicted PhP RE by the developed models.

Component	Source of variation	SS ^a	df ^b	MS ^c	F _{ratio}	P-value	F _{critical}
$RE_{predicted}$	Between groups	0.0073	2	0.0036	0.0487	0.9524	3.0212
	Within groups	26.5357	354	0.0749			
	Total	26.5430	356				

^a Sum of squares.

^b Degrees of freedom.

^c Mean squares.

predictive way for modeling of any other reactor configuration for photocatalytic ozonation of the pollutants as well as photoreactor design or scaling-up objectives. The empirical model developed on the basis of the effect of main influencing parameters of the system is a simple method and able to show the effect, the contribution and the number of the main key factors involved in the process. Using the empirical model it is possible to identify the insignificant and notable main factors. This can reduce the complexity of the system. On the other hand, in this approach, the range of all factors should be determined properly. ANNs have been proposed as a powerful tool for modeling non-linear multivariate systems. The important advantages of ANN in comparison with intrinsic kinetic modeling

are that ANN does not need a former knowledge about the process mechanism. In other words, there is no need for mathematical explanation of the reactions occurred in the system. ANNs are able to fit and model all types of non-linear functions from presentation of experimental inputs

4. Conclusions

Degradation of PhP in aqueous solution by heterogeneous photocatalytic ozonation in the presence of TiO_2 nanoparticles thin film was modeled with intrinsic kinetic, empirical kinetic and ANN approaches. TiO_2 nanoparticles were immobilized on the surface

of ceramic plates through a sol-gel based method. The SEM images demonstrated that the produced TiO₂ thin film was homogeneous and crack-free on the entire surface. AFM results elucidated that the immobilized TiO₂ thin film was composed of uniform distribution of aggregated nanoclusters of 27.2 nm, which were arranged meticulously with a 27.2 nm distance. The kinetic characteristics of the photocatalytic ozonation of PhP were experimentally investigated with respect to the pH, initial PhP concentration and ozone inlet flow rate. Then, a novel intrinsic kinetic model was proposed to predict the PhP removal efficiency in photocatalytic ozonation process. The developed model was validated by using the experimental data as well as the error functions. The model predictions agreed reasonably well with the experimental data (R^2 value of 0.987, MSE value of 0.0011 and MAE value of 0.0290). The model could also well explain the effect of the initial PhP concentration, light intensity and dissolved ozone and oxygen concentrations on the degradation rate constant. In order to further investigate the accuracy of the developed model, the empirical kinetic model on the basis of the main operational parameters and ANN using feed-forward back propagation network with trainscg algorithm and topology (5: 14: 1) were established. By using the developed empirical and ANN models a good agreement between the predicted PhP removal efficiencies and the experimental results were also achieved (R^2 values were 0.982 and 0.993 for the empirical kinetic model and ANN, respectively). ANOVA elucidated that there was no significant difference among the predicting capability of the three models. The present issue indicated that the intrinsic kinetic model was rationally deduced on the basis of correct reactions involved in the process and valid assumptions. As a consequence, this study enabled relevant modeling approaches to design and analysis of complex systems aiming proper application of heterogeneous photocatalytic ozonation in industry.

Acknowledgments

The authors sincerely thank to the University of Tabriz (Iran) for all the support.

Appendix A. Supplementary data

Supplementary data associated with this article can be found, in the online version, at <http://dx.doi.org/10.1016/j.apcatb.2015.11.033>.

References

- [1] G. Márquez, E.M. Rodríguez, F.J. Beltrán, P.M. Álvarez, *Chemosphere* 113 (2014) 71–78.
- [2] T.A. Larsen, J. Lienert, A. Joss, H. Siegrist, *J. Biotechnol.* 113 (2004) 295–304.
- [3] M. Fathinia, A. Khataee, A. Naseri, S. Aber, *Spectrochim. Acta, Part A* 136 (2015) 1275–1290, Part C.
- [4] V. Homem, L. Santos, *J. Environ. Manage.* 92 (2011) 2304–2347.
- [5] M. Fathinia, A. Khataee, *Appl. Catal. A-Gen.* 491 (2015) 136–154.
- [6] A.R. Khataee, M. Fathinia, S.W. Joo, *Spectrochim. Acta Part A* 112 (2013) 33–45.
- [7] A.R. Khataee, M. Safarpour, M. Zarei, S. Aber, *J. Molecul. Catal. A-Chem.* 363 (2012) 58–68.
- [8] M. Addamo, V. Augugliaro, E. García-López, V. Loddo, G. Marcì, L. Palmisano, *Catal. Today* 107–108 (2005) 612–618.
- [9] M. Mehrjouei, S. Müller, D. Möller, *Chem. Eng. J.* 263 (2015) 209–219.
- [10] F.J. Beltrán, A. Aguinaco, J.F. García-Araya, *Appl. Catal. B-Environ.* 100 (2010) 289–298.
- [11] D.H. Quiñones, A. Rey, P.M. Álvarez, F.J. Beltrán, P.K. Plucinski, *Appl. Catal. B-Environ.* 144 (2014) 96–106.
- [12] E. Mena, A. Rey, B. Acedo, F.J. Beltrán, S. Malato, *Chem. Eng. J.* 204–206 (2012) 131–140.
- [13] E.M. Rodríguez, G. Márquez, E.A. León, P.M. Álvarez, A.M. Amat, F.J. Beltrán, *J. Environ. Manage.* 127 (2013) 114–124.
- [14] M. Ye, Z. Chen, X. Liu, Y. Ben, J. Shen, J. Hazard. Mater. 167 (2009) 1021–1027.
- [15] F.J. Beltrán, A. Aguinaco, A. Rey, J.F. García-Araya, *Ind. Eng. Chem. Res.* 51 (2012) 4533–4544.
- [16] S. Dong, D. Zhou, X. Bi, *Particuology* 8 (2010) 60–66.
- [17] R.C. Martins, R.J.G. Lopes, R.M. Quint-Ferreira, *Chem. Eng. J.* 165 (2010) 678–685.
- [18] A.R. Amani-Ghadim, M.S.S. Dorraji, *Appl. Catal. B-Environ.* 163 (2015) 539–546.
- [19] A.R. Khataee, M. Fathinia, S. Aber, M. Zarei, *J. Hazard. Mater.* 181 (2010) 886–897.
- [20] J. Marugan, R. Vangrieken, A. Cassano, O. Alfano, *Appl. Catal. B-Environ.* 85 (2008) 48–60.
- [21] C. Shen, Y.J. Wang, J.H. Xu, G.S. Luo, *Chem. Eng. J.* 209 (2012) 478–485.
- [22] A.R. Khataee, M. Fathinia, S. Aber, *Ind. Eng. Chem. Res.* 49 (2010) 12358–12364.
- [23] H. Bader, J. Hoigné, *Water Res.* 15 (1981) 449–456.
- [24] U. Cernigoj, U.L. Štangar, P. Trebše, *Appl. Catal. B-Environ.* 75 (2007) 229–238.
- [25] F.J. Beltrán, A. Aguinaco, J.F. García-Araya, *Water Res.* 43 (2009) 1359–1369.
- [26] G. Márquez, E.M. Rodríguez, F.J. Beltrán, P.M. Álvarez, *Chemosphere* 113 (2014) 71–78.
- [27] F.J. Beltrán, J.P. Pocostales, P.M. Alvarez, J. Jaramillo, *J. Hazard. Mater.* 169 (2009) 532–538.
- [28] F.J. Beltrán, F.J. Rivas, R. Montero-de-Espinosa, *Appl. Catal. B- Environ.* 39 (2002) 221–231.
- [29] S.-N. Zhu, K.N. Hui, X. Hong, K.S. Hui, *Chem. Eng. J.* 242 (2014) 180–186.
- [30] E. Mvula, C. von Sonntag, *Org. Biomol. Chem.* 1 (2003) 1749–1756.
- [31] A.R. Khataee, M. Fathinia, in: S.L. Stib (Ed.), *New and Future Developments in Catalysis*, Elsevier Science, BV, Amsterdam, 2013, pp. 267–288.
- [32] S. Brosillon, L. Lhomme, C. Vallet, A. Bouzaza, D. Wolbert, *Appl. Catal. B-Environ.* 78 (2008) 232–241.
- [33] S. Dutta, S.A. Parsons, C. Bhattacharjee, P. Jarvis, S. Datta, S. Bandyopadhyay, *Chem. Eng. J.* 155 (2009) 674–679.
- [34] G. Rothenberger, J. Moser, M. Graetzel, N. Serpone, D.K. Sharma, *J. Am. Chem. Soc.* 107 (1985) 8054–8059.
- [35] Y. Li, S. Sun, M. Ma, Y. Ouyang, W. Yan, *Chem. Eng. J.* 142 (2008) 147–155.
- [36] D.F. Ollis, E. Pelizzetti, N. Serpone, *Environ. Sci. Technol.* 25 (1991) 1522–1529.
- [37] H. Zheng, S. Fang, H. Lou, Y. Chen, L. Jiang, H. Lu, *Exp. Syst. Appl.* 38 (2011) 5591–5602.
- [38] E.S. Elmolla, M. Chaudhuri, M.M. Eltoukhy, *J. Hazard. Mater.* 179 (2010) 127–134.
- [39] A.R. Khataee, M.B. Kasiri, *J. Mol. Catal. A-Chem.* 331 (2010) 86–100.
- [40] M. Huang, Y. Ma, J. Wan, H. Zhang, Y. Wang, Y. Chen, C. Yoo, W. Guo, *Bioresour. Technol.* 102 (2011) 8907–8913.
- [41] A.R. Khataee, M. Fathinia, M. Zarei, B. Izadkhah, S.W. Joo, *J. Ind. Eng. Chem.* 20 (2014) 1852–1860.